The Astronomical Journal, 152:161 (16pp), 2016 December doi:10.3847/0004-6256/152/6/161

HATS-31B THROUGH HATS-35B: FIVE TRANSITING HOT JUPITERS DISCOVERED BY THE HATSOUTH SURVEY*

M. de Val-Borro[1], G. Á. Bakos[1,14,15], R. Brahm[2,3], J. D. Hartman[1], N. Espinoza[2,3], K. Penev[1], S. Ciceri[4,5], A. Jordán[2,3], W. Bhatti[1], Z. Csubry[1], D. Bayliss[6], J. Bento[7], G. Zhou[8], M. Rabus[2,4], L. Mancini[4], T. Henning[4], B. Schmidt[7], T. G. Tan[9], C. G. Tinney[10,11], D. J. Wright[10,11], L. Kedziora-Chudczer[10,11], J. Bailey[10,11], V. Suc[2], S. Durkan[12], J. Lázár[13], I. Papp[13], and P. Sári[13]

[1] Department of Astrophysical Sciences, Princeton University, NJ 08544, USA
[2] Instituto de Astrofísica, Facultad de Física, Pontificia Universidad Católica de Chile, Av. Vicuña Mackenna 4860, 7820436 Macul, Santiago, Chile
[3] Millennium Institute of Astrophysics, Av. Vicuña Mackenna 4860, 782-0436 Macul, Santiago, Chile
[4] Max Planck Institute for Astronomy, Königstuhl 17, D-69117 Heidelberg, Germany
[5] Department of Astronomy, Stockholm University, SE-10691 Stockholm, Sweden
[6] Observatoire Astronomique de l'Université de Geneve, 51 ch. des Maillettes, 1290 Versoix, Switzerland
[7] Research School of Astronomy and Astrophysics, Australian National University, Canberra, ACT 2611, Australia
[8] Harvard-Smithsonian Center for Astrophysics, 60 Garden Street, Cambridge, MA 02138, USA
[9] Perth Exoplanet Survey Telescope, Perth, Australia
[10] Exoplanetary Science at UNSW, School of Physics, University of New South Wales, Sydney, NSW 2052, Australia
[11] Australian Centre for Astrobiology, University of New South Wales, Sydney, NSW 2052, Australia
[12] Astrophysics Research Centre, School of Mathematics & Physics, Queen's University, Belfast BT7 1NN, UK
[13] Hungarian Astronomical Association, 1451 Budapest, Hungary
Received 2016 June 24; accepted 2016 July 31; published 2016 November 11

ABSTRACT

We report the discovery of five new transiting hot-Jupiter planets discovered by the HATSouth survey, HATS-31b through HATS-35b. These planets orbit moderately bright stars with V magnitudes within the range of 11.9–14.4 mag while the planets span a range of masses of 0.88–1.22 M_J and have somewhat inflated radii between 1.23 and 1.64 R_J. These planets can be classified as typical hot Jupiters, with HATS-31b and HATS-35b being moderately inflated gas giant planets with radii of $1.64 \pm 0.22\ R_J$ and $1.464^{+0.069}_{-0.044}\ R_J$, respectively, that can be used to constrain inflation mechanisms. All five systems present a higher Bayesian evidence for a fixed-circular-orbit model than for an eccentric orbit. The orbital periods range from 1.8209993 ± 0.0000016 day for HATS-35b) to 3.377960 ± 0.000012 day for HATS-31b. Additionally, HATS-35b orbits a relatively young F star with an age of 2.13 ± 0.51 Gyr. We discuss the analysis to derive the properties of these systems and compare them in the context of the sample of well-characterized transiting hot Jupiters known to date.

Key words: planetary systems – stars: individual – techniques: photometric – techniques: spectroscopic

Supporting material: machine-readable table

1. INTRODUCTION

Planets that eclipse their host star during their orbit are key objects for the study of exoplanetary systems. The special geometry of transiting extrasolar planets (TEPs) enables measurements of, not only the planet size, but other important physical parameters, such as their masses and densities as well as the characterization of the alignment between the orbital axis of a planet and the spin axis of its host star through the Rossiter–McLaughlin effect. The majority of well-characterized TEPs have been discovered by wide-field photometric surveys, including *Kepler* (Borucki et al. 2010), the Wide Angle Search for Planets (Pollacco et al. 2006), the Hungarian-made Automated Telescope Network (HATNet; Bakos et al. 2004, 2013), COnvection ROtation and planetary Transits (CoRoT; Barge et al. 2008), and the Kilodegree Extremely Little Telescope survey (Siverd et al. 2012).

The known sample of exoplanets presents a great diversity of orbital and planetary parameters. Extending the sample of close-orbiting TEPs is a key goal of ground-based surveys because they allow for a large array of additional observational measurements, such as information about the chemical composition of the atmospheres of the planets using emission and transmission spectroscopy for sufficiently bright targets. The HATSouth survey (Bakos et al. 2013) has been designed to increase the sample of well-characterized TEPs. Some recent examples of planets discovered by HATSouth are HATS-18b (Penev et al. 2016) and HATS-25b through HATS-30b (Espinoza et al. 2016). A full list of TEPs discovered by the HATSouth survey, along with all discovery and follow-up light curves, can be found at http://hatsouth.org/.

In this paper, we present five new transiting planets discovered by the HATSouth network around moderately bright stars: HATS-31b through HATS-35b. In Section 2, we describe the photometric transit detection with HATSouth, as well as the data analysis methods and the procedures used to confirm the planetary nature of the transit signal using follow-

* The HATSouth network is operated by a collaboration consisting of Princeton University (PU), the Max Planck Institute für Astronomie (MPIA), the Australian National University (ANU), and the Pontificia Universidad Católica de Chile (PUC). The station at Las Campanas Observatory (LCO) of the Carnegie Institute is operated by PU in conjunction with PUC, the station at the High Energy Spectroscopic Survey (H.E.S.S.) site is operated in conjunction with MPIA, and the station at Siding Spring Observatory (SSO) is operated jointly with ANU. Based in part on data collected at the Subaru Telescope, which is operated by the National Astronomical Observatory of Japan. Based in part on observations made with the MPG 2.2 m and *Euler*1.2 m Telescopes at the ESO Observatory in La Silla. This paper uses observations obtained with facilities of the Las Cumbres Observatory Global Telescope.

[14] Alfred P. Sloan Research Fellow.

[15] Packard Fellow.

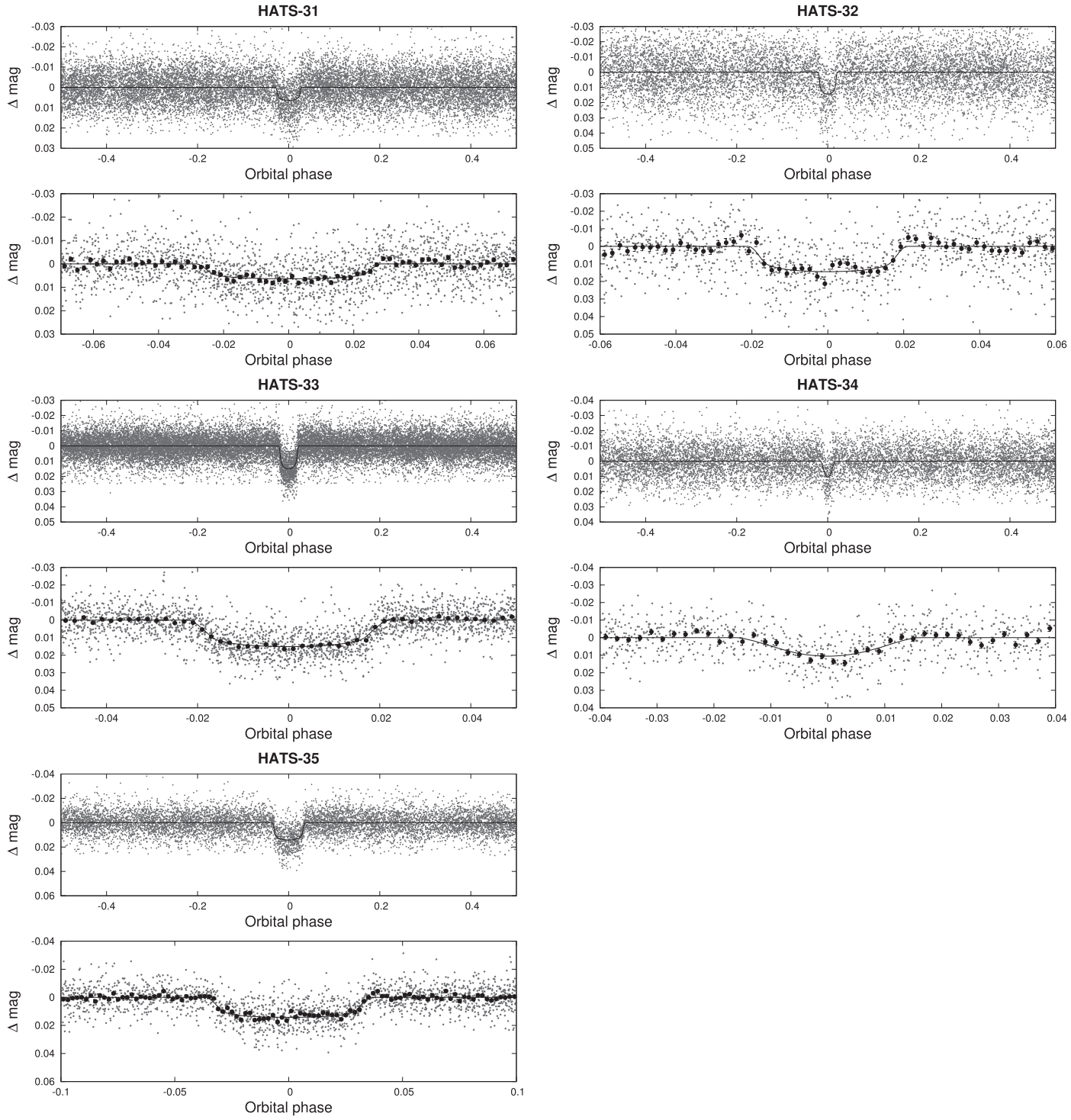

Figure 1. Phase-folded unbinned HATSouth light curves for the five new transiting planet systems. In each case, we show two panels. The top panel shows the full light curve, while the bottom panel shows the light curve zoomed-in on the transit. The solid lines show the model fits to the light curves. The dark filled circles in the bottom panels show the light curves binned in phase with a bin size of 0.002.

up spectroscopic and photometric observations. In Section 3, we describe the analysis carried out to rule out false positive scenarios that could mimic a planetary signal, and to ascertain the stellar and planetary parameters. We discuss the implication of our results and compare them with all known transiting hot Jupiters to date in Section 4.

2. OBSERVATIONS

2.1. Photometric Detection

The HATSouth survey is a global network of homogeneous, completely automated wide-field telescopes located at three sites in the Southern Hemisphere: the Las Campanas Observa-

Table 1
Summary of Photometric Observations

Instrument/Field[a]	Date(s)	# Images	Cadence[b] (sec)	Filter	Precision[c] (mmag)
HATS-31					
HS-1.4/G565	2012 Dec–2013 Jun	5750	282	r	8.0
HS-3.4/G565	2012 Dec–2013 Jul	3850	280	r	8.1
HS-5.4/G565	2012 Dec–2013 Jul	5187	287	r	7.5
LCOGT 1 m+CTIO/sinistro	2015 Feb 28	53	226	i	1.1
LCOGT 1 m+SAAO/SBIG	2015 Mar 06	137	139	i	3.6
Swope 1 m/e2v	2015 Apr 02	281	54	i	4.0
HATS-32					
HS-2.3/G586	2010 Aug–2011 Nov	4159	290	r	14.9
HS-4.3/G586	2010 Aug–2011 Nov	4510	298	r	14.1
HS-6.3/G586	2010 Aug–2011 Nov	498	293	r	14.4
PEST 0.3 m	2014 Jul 09	145	133	R_C	10.5
DK 1.54 m/DFOSC	2014 Nov 04	120	145	R	2.0
Swope 1 m/e2v	2015 May 28	53	189	i	6.6
HATS-33					
HS-1.4/G747	2013 Mar–2013 Oct	4271	287	r	6.4
HS-2.4/G747	2013 Sep–2013 Oct	1280	287	r	9.6
HS-3.4/G747	2013 Apr–2013 Nov	8813	297	r	7.8
HS-4.4/G747	2013 Sep–2013 Nov	1531	297	r	8.7
HS-5.4/G747	2013 Mar–2013 Nov	6049	297	r	5.9
HS-6.4/G747	2013 Sep–2013 Nov	1557	290	r	9.0
LCOGT 1 m+CTIO/sinistro	2015 May 20	128	48	i	4.7
HATS-34					
HS-2.4/G754	2012 Sep–2012 Dec	3805	282	r	9.1
HS-4.4/G754	2012 Sep–2013 Jan	2865	292	r	10.0
HS-6.4/G754	2012 Sep–2012 Dec	2975	285	r	9.9
PEST 0.3 m	2014 Oct 26	54	211	R_C	5.3
DK 1.54 m/DFOSC	2014 Nov 03	97	125	R	1.3
AAT 3.9 m/IRIS2[d]	2015 Sep 25	715	10	K_S	8.1
HATS-35					
HS-2.4/G778	2011 May–2012 Nov	3013	287	r	9.6
HS-4.4/G778	2011 Jul–2012 Nov	3699	298	r	7.5
HS-6.4/G778	2011 Apr–2012 Oct	2294	298	r	8.5
LCOGT 1 m+CTIO/sinistro	2015 Jun 12	38	163	i	1.2
LCOGT 1 m+SAAO/SBIG	2015 Jul 14	19	144	i	0.8
LCOGT 1 m+CTIO/sinistro	2015 Jul 15	79	162	i	1.1
LCOGT 1 m+SSO/SBIG	2015 Jul 18	106	133	i	1.6
LCOGT 1 m+CTIO/sinistro	2015 Jul 24	105	162	i	0.8

Notes.
[a] For HATSouth data, we list the HATSouth unit, CCD and field name from which the observations are taken. HS-1 and -2 are located at Las Campanas Observatory in Chile, HS-3 and -4 are located at the H.E.S.S. site in Namibia, and HS-5 and -6 are located at Siding Spring Observatory in Australia. Each unit has 4 ccds. Each field corresponds to one of 838 fixed pointings used to cover the full 4π celestial sphere. All data from a given HATSouth field and CCD number are reduced together, while detrending through External Parameter Decorrelation (EPD) is done independently for each unique unit+CCD+field combination.
[b] The median time between consecutive images rounded to the nearest second. Due to factors such as weather, the day–night cycle, guiding, and focus corrections, the cadence is only approximately uniform over short timescales.
[c] The rms of the residuals from the best-fit model.
[d] This light curve covers a predicted secondary eclipse event, it is not included in the analysis carried out to determine the system parameters for HATS-34; however, it is included in the analysis carried out to exclude blend scenarios.

tory (LCO) in Chile, the High Energy Stereoscopic Survey (H.E.S.S.) site in Namibia, and the Siding Spring Observatory (SSO) in Australia. Observations are performed using a Sloan-r filter with four-minute exposures. The HATSouth network was commissioned in 2009 and since then has proved to be a robust system for the monitoring of time-variable phenomena. Each HATSouth unit consists of four Takahashi E180 astrographs with an aperture of 18 cm and an $f/2.8$ focal ratio on a common mount, equipped with Apogee 4096×4096 U16M ALTA cameras. The observations and aperture photometry reduction pipeline used by the HATSouth survey have been described comprehensively in Bakos et al. (2013) and Penev et al. (2013).

Below, we describe specific details of the observations leading to the discovery of HATS-31b, HATS-32b, HATS-33b, HATS-34b, and HATS-35b. The HATSouth raw data were reduced to trend-filtered light curves using the External Parameter Decorrelation method (EPD; Bakos et al. 2010) and the Trend Filtering Algorithm (TFA; Kovács et al. 2005) to correct for systematic variations in the photometry before searching for transit signals. We searched the light curves for

Table 2
Summary of Spectroscopy Observations

Instrument	UT Date(s)	# Spec.	Res. $\Delta\lambda/\lambda/1000$	S/N Range[a]	γ_{RV}[b] (km s^{-1})	RV Precision[c] (m s^{-1})
HATS-31						
ANU 2.3 m/WiFeS	2014 Dec 30–31	2	7	45–56	−9.3	4000
ANU 2.3 m/WiFeS	2015 Jan 1	1	3	77	...	...
ESO 3.6 m/HARPS	2015 Feb 14–19	6	115	12–22	−8.705	17
HATS-32						
ANU 2.3 m/WiFeS	2014 Jun 3–5	3	7	19–61	9.1	4000
ANU 2.3 m/WiFeS	2014 Jun 4	1	3	69	...	...
MPG 2.2 m/FEROS	2014 Jul–2015 Jun	8	48	20–45	12.423	30
HATS-33						
ANU 2.3 m/WiFeS	2014 Dec–2015 Mar	4	7	51–71	11.420	4000
ANU 2.3 m/WiFeS	2015 Mar 4	1	3	44	...	...
Euler 1.2 m/Coralie	2015 Mar–Jun	5	60	18–25	11.056	42
ESO 3.6 m/HARPS	2015 Apr 6–8	3	115	19–27	11.077	2
AAT 3.9 m/CYCLOPS2	2015 May 7–13	11	70	17–44	11.066	23
MPG 2.2 m/FEROS	2015 May–Jul	4	48	40–73	11.057	38
HATS-34						
ANU 2.3 m/WiFeS	2014 Oct 4	1	3	50	...	...
ANU 2.3 m/WiFeS	2014 Oct 4–10	3	7	55–95	16.4	4000
MPG 2.2 m/FEROS[d]	2015 Jun–Jul	10	48	16–43	17.734	23
HATS-35						
ANU 2.3 m/WiFeS	2014 Oct 5	1	3	99	...	...
ANU 2.3 m/WiFeS	2014 Oct 11	1	7	102	−14.3	4000
Euler 1.2 m/Coralie	2014 Nov–2015 Jun	5	60	16–21	−14.173	110
ESO 3.6 m/HARPS	2015 Apr 7–8	2	115	15–23	−14.245	42
MPG 2.2 m/FEROS	2015 Jun–Jul	10	48	41–63	−14.185	20

Notes.
[a] S/N per resolution element near 5180 Å.
[b] For high-precision radial velocity observations included in the orbit determination, this is the zero-point velocity from the best-fit orbit. For other instruments, it is the mean value. We do not provide this quantity for the lower resolution WiFeS observations, which were only used to measure stellar atmospheric parameters.
[c] For high-precision radial velocity observations included in the orbit determination, this is the scatter in the residuals from the best-fit orbit (which may include astrophysical jitter); for other instruments, this is either an estimate of the precision (not including jitter) or the measured standard deviation. We do not provide this quantity for low-resolution observations from the ANU 2.3 m/WiFeS.
[d] Three of the MPG 2.2 m/FEROS observations of HATS-34 were excluded from the analysis due to having low S/N or high sky contamination.

periodic box-shaped signals using the Box-fitting Least-Squares (BLS; Kovács et al. 2002) algorithm, and detected periodic transit signals in the light curves as shown in Figure 1. The reduced data are available in Table 3. We summarize below the transits detected in the light curves of the stars HATS-31 through HATS-35.

1. *HATS-31* (2MASS 12464866-2425385; $\alpha = 12^h46^m48^s.72$, $\delta = -24°25'38''.5$; J2000; V = 13.105 ± 0.030). A signal was detected with an apparent depth of ∼6.1 mmag at a period of $P =$ 3.3780 day.
2. *HATS-32* (2MASS 23041801-2116189; $\alpha = 23^h04^m18^s.12$, $\delta = -21°16'19''.0$; J2000; V = 14.384 ± 0.010). A signal was detected with an apparent depth of ∼15.3 mmag at a period of $P = 2.8127$ day.
3. *HATS-33* (2MASS 19383207-5519483; $\alpha = 19^h38^m31^s.92$, $\delta = -55°19'48''.4$; J2000; V = 11.911 ± 0.070). A signal was detected with an apparent depth of ∼14.0 mmag at a period of $P = 2.5496$ day.
4. *HATS-34* (2MASS 00030587-6228096; $\alpha = 00^h03^m05^s.88$, $\delta = -62°28'09''.6$; J2000; V=13.849 ± 0.010). A signal was detected with an apparent depth of ∼13.4 mmag at a period of $P = 2.1062$ day.
5. *HATS-35* (2MASS 19464518-6333561; $\alpha = 19^h46^m45^s.12$, $\delta = -63°33'56''.2$; J2000; V = 12.56 ± 0.10). A signal was detected with an apparent depth of ∼13.1 mmag at a period of $P = 1.8210$ day.

Subsequent spectroscopic and photometric follow-up observations for the five systems were carried out to confirm the transit signal and the planetary nature of these objects as described in the following sections.

2.2. Spectroscopic Observations

In Table 2, we summarize all spectroscopic observations taken for HATS-31 to HATS-35.

2.2.1. Reconnaissance Spectroscopy

To exclude stellar binary false positives and confirm planetary candidates detected by the HATSouth network, we carry out initial low- and medium-resolution reconnaissance spectroscopy before attempting higher precision observations to determine orbital parameters. These reconnaissance observations consist of spectral typing observations of all the objects using the Wide Field Spectrograph (WiFeS) on the ANU 2.3 m telescope at SSO. The observing strategy and data reduction procedure for WiFeS data are described in detail in Bayliss et al. (2013). The number of medium- and low-resolution spectra obtained for each system are summarized in Table 2. HATS-31 through HATS-35

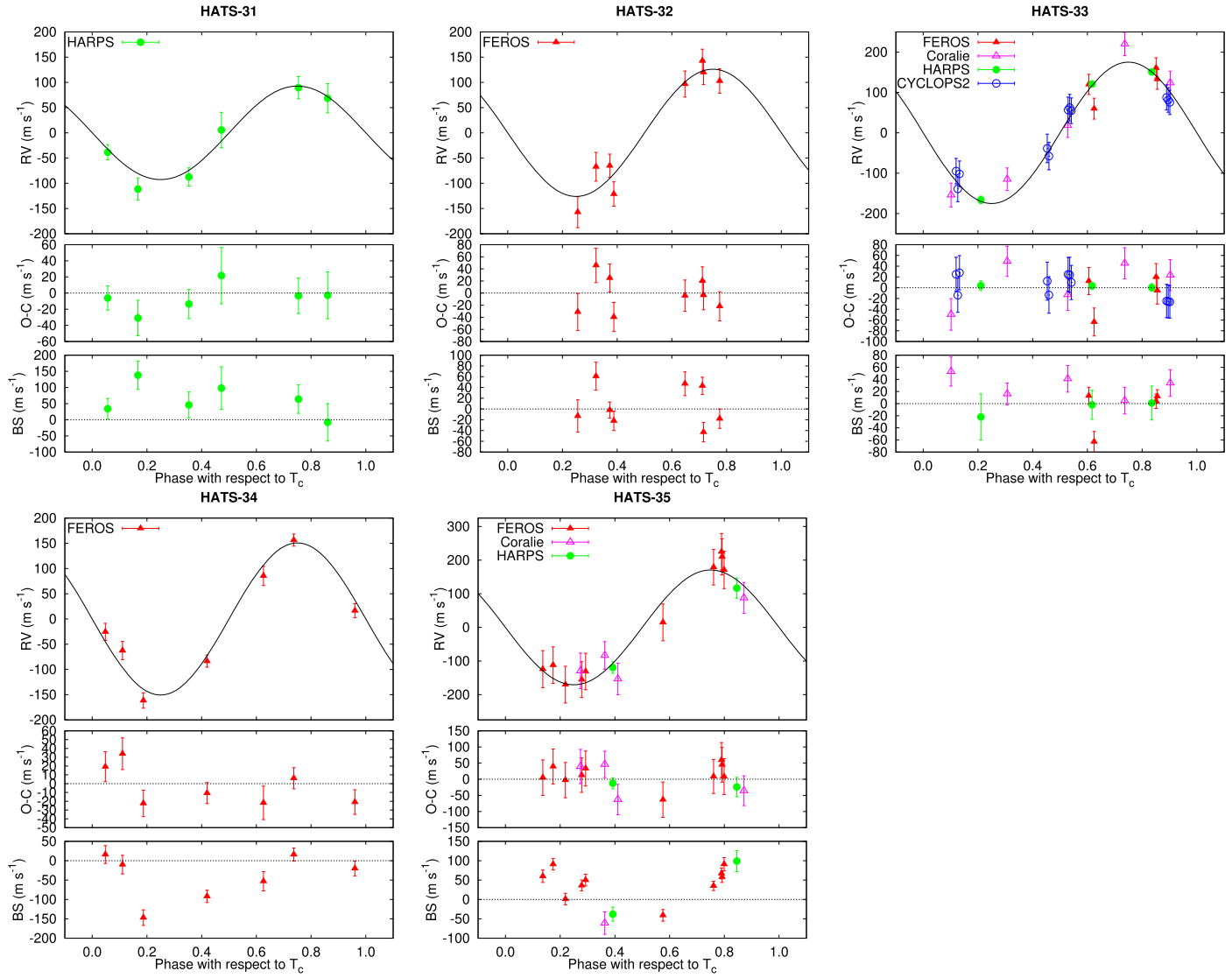

Figure 2. Phased high-precision radial velocity measurements for the five new transiting planet systems. The instruments used are labelled in the plots. In each case, we show three panels. The top panel shows the phased measurements together with our best-fit circular-orbit model for HATS-31 through HATS-35 (see Table 6). Zero-phase corresponds to the time of mid-transit. The center-of-mass velocity has been subtracted. The second panel shows the velocity $O-C$ residuals from the best fit. The error bars include the jitter terms listed in Tables 6 and 7 added in quadrature to the formal errors for each instrument. The third panel shows the bisector spans. Note the different vertical scales of the panels.

were confirmed as single-lined stars by these WiFeS observations. Using these low-resolution spectra, we obtained approximate stellar atmospheric parameters that indicate HATS-31 is an F-type star, while HATS-32 through HATS-35 are G-type stars. Medium-resolution WiFeS observations with spectral resolution $R = \lambda/\Delta\lambda = 7000$ are then used to rule out possible eclipsing stellar companions in any of these systems by measuring no radial velocity variations in excess of $\sim$5 km s^{-1}.

2.2.2. *High-resolution Spectroscopy*

Following reconnaissance spectroscopy to reject possible false positives like blended binary systems and to obtain first estimates of stellar parameters, stable and high-precision spectroscopic measurements are obtained to collect high-precision radial velocity (RV) variations and line bisector (BS) time series for each of the candidates. Several high-resolution spectra were acquired for these objects with a combination of the FEROS (Kaufer & Pasquini 1998), HARPS (Mayor et al. 2003), Coralie (Queloz et al. 2001), and CYCLOPS2+UCLES spectrographs (Horton et al. 2012) between 2014 July and 2015 July.

Altogether, we obtained 11 spectra using CYCLOPS2 +UCLES at the 3.9 m Anglo-Australian Telescope (AAT), 11 spectra using HARPS at the ESO 3.6 m telescope, 10 spectra using CORALIE at the Euler 1.2 m telescope, and 32 spectra with FEROS at the MPG 2.2 m telescope. The data from the FEROS, HARPS, and Coralie instruments were reduced homogeneously with an automated pipeline for echelle spectrographs described in detail in Jordán et al. (2014). The CYCLOPS2 observations were reduced and analyzed following Addison et al. (2013). Combined high-precision RV and BS measurements are shown for each system folded with the period of the transit signal in Figure 2. Note that BS measurements from CYCLOPS2 for HATS-33 are missing

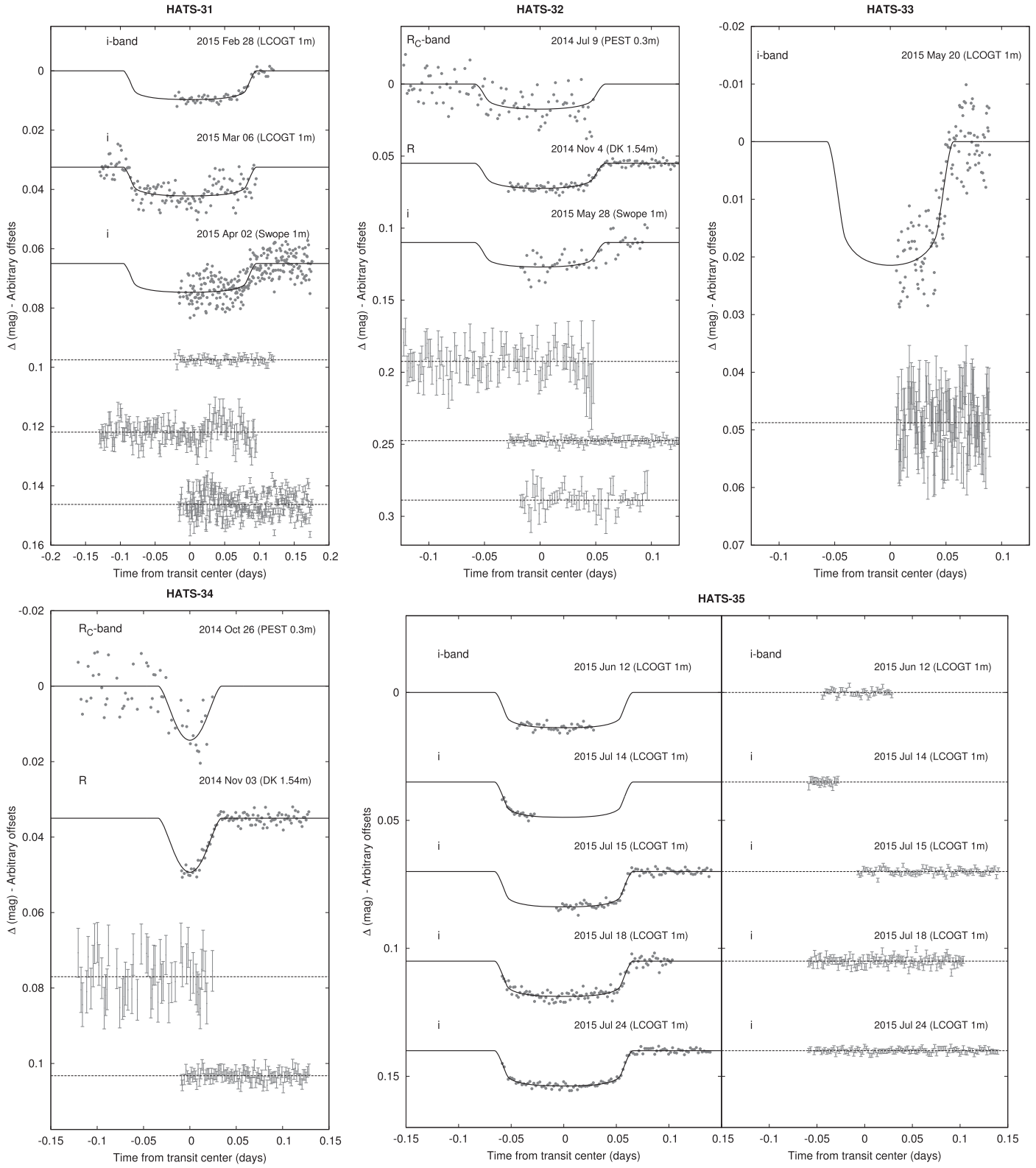

Figure 3. Unbinned transit light curves for HATS-31 through HATS-35. The light curves have been corrected for quadratic trends in time fitted simultaneously with the transit model, and for correlations with up to three parameters describing the shape of the PSF. The dates of the events, filters, and instruments used are indicated. Light curves following the first are displaced vertically for clarity. Our best fit from the global modeling described in Section 3.3 is shown by the solid lines. For HATS-31 through HATS-34, the residuals from the best-fit model are shown below in the same order as the original light curves, for HATS-35 the residuals are shown to the right of the light curves. The error bars represent the photon and background shot noise, plus the readout noise. Note the differing vertical and horizontal scales used for each system.

due to not having a BS pipeline for this instrument. The high-resolution spectroscopic data are provided in Table 8 at the end of the paper.

All the candidates show clear sinusoidal variation in RV that are in phase with the observed transits. From these observations, we estimate orbital parameters, as well as confirm the

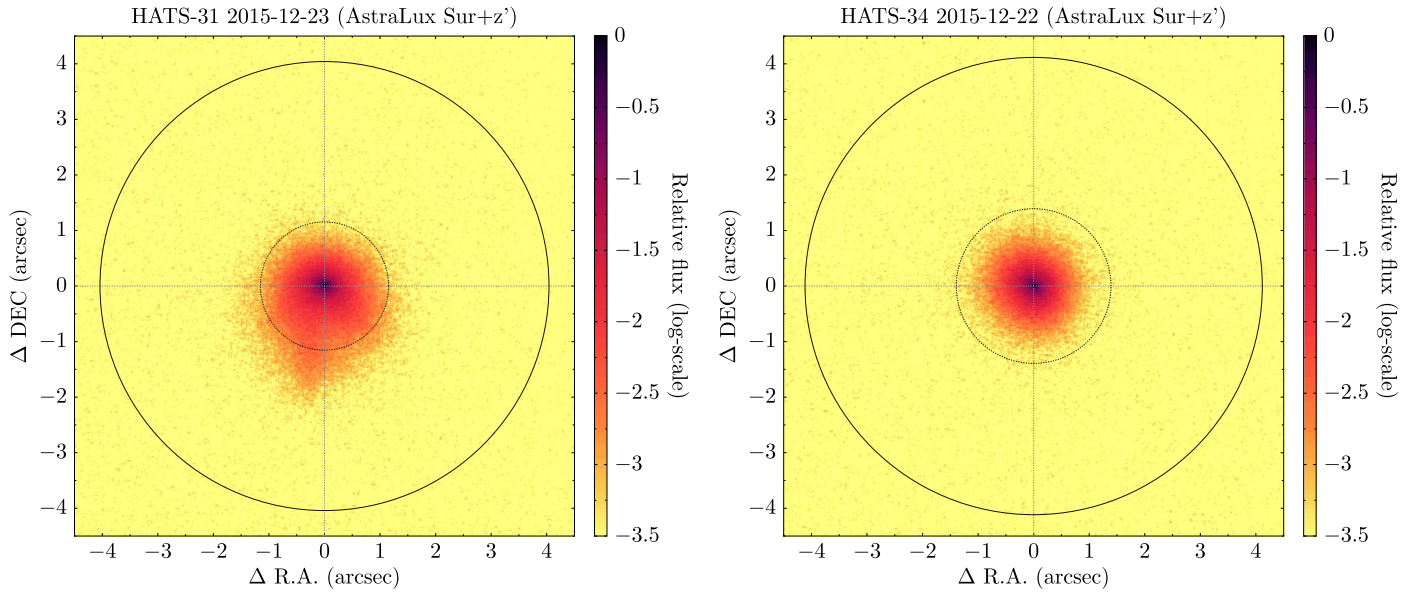

Figure 4. Sloan z'-band images for HATS-31 and HATS-34 obtained with the AstraLux Sur camera. Circles of $1''$ radius and $5''$ radius are shown for reference on the images. Note the difference in the shape of the PSF.

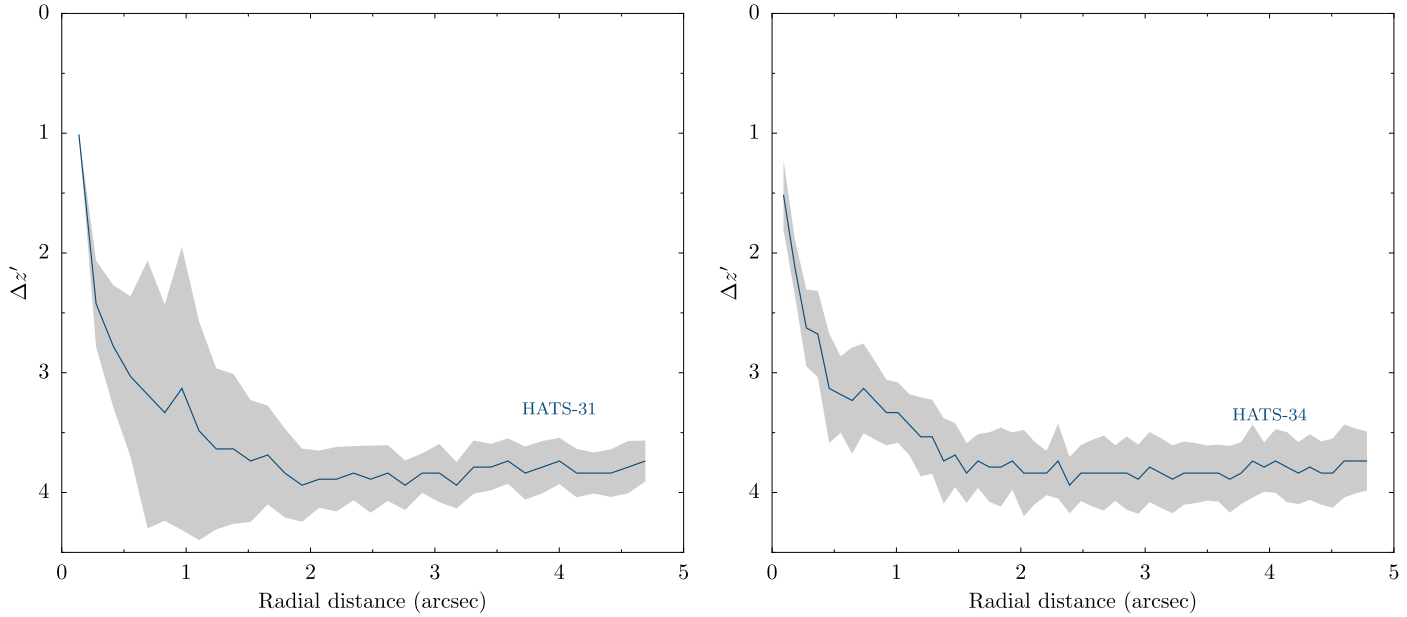

Figure 5. Contrast curves for HATS-31 (left panel) and HATS-34 (right panel) based on observations with the Astralux Sur camera using the Sloan z' filter shown in Figure 4. The gray bar shows the 1σ uncertainty of the contrast at each radius.

mass of the companion for systems that host planets, and measure precisely the stellar atmospheric parameters.

2.3. Photometric Follow-up Observations

To obtain higher precision light curves of the transit event, we photometrically followed up all the planets using facilities with larger apertures than the HATSouth telescopes. Photometric follow-up observations are summarized in Table 1, including the cadence, filter, and photometric precision, and plotted in Figure 3. For all objects, the follow-up light curves were consistent with the discovery observations. These observations allow us to refine the transit ephemeris of the systems and their physical parameters.

The egress of HATS-31b was observed on 2015 February 28 and 2015 April 02 with the Las Cumbres Observatory Global Telescope (LCOGT) 1 m telescope network (Brown et al. 2013) and the Swope 1 m telescopes, respectively. Additionally, an almost full transit of HATS-31b was observed with LCOGT on 2015 March 6. Another three partial transits of HATS-32b were observed with the PEST 0.3 m, DK 1.54 m, and the Swope 1 m telescopes. The egress of HATS-33 was measured with the 1 m LCOGT at CTIO on 2015 May 20. Both ingress and egress of HATS-34b were observed by the PEST 0.3 m and DK 1.54 m

Table 3
Light-curve Data for HATS-31–HATS-35

Object[a]	BJD[b] (2,400,000+)	Mag[c]	$\sigma_{\rm Mag}$	Mag(orig)[d]	Filter	Instrument
HATS-31	56441.63105	0.00775	0.00473	⋯	*r*	HS
HATS-31	56330.15845	−0.00143	0.00435	⋯	*r*	HS
HATS-31	56424.74146	0.00333	0.00446	⋯	*r*	HS
HATS-31	56448.38748	−0.00568	0.00425	⋯	*r*	HS
HATS-31	56357.18277	0.01570	0.00450	⋯	*r*	HS
HATS-31	56417.98607	−0.00175	0.00432	⋯	*r*	HS
HATS-31	56404.47434	−0.00078	0.00556	⋯	*r*	HS
HATS-31	56401.09654	−0.00630	0.00440	⋯	*r*	HS
HATS-31	56414.60840	0.00526	0.00417	⋯	*r*	HS
HATS-31	56390.96315	−0.00847	0.00457	⋯	*r*	HS

Notes.
[a] Either HATS-31, HATS-32, HATS-33, HATS-34, or HATS-35.
[b] Barycentric Julian Date is computed directly from the UTC time without correction for leap seconds.
[c] The out-of-transit level has been subtracted. For observations made with the HATSouth instruments (identified by "HS" in the "Instrument" column), these magnitudes have been corrected for trends using the EPD and TFA procedures applied prior to fitting the transit model. This procedure may lead to an artificial dilution in the transit depths. The blend factors for the HATSouth light curves are listed in Tables 6 and 7. For observations made with follow-up instruments (anything other than "HS" in the "Instrument" column), the magnitudes have been corrected for a quadratic trend in time, and for variations correlated with three PSF shape parameters, fit simultaneously with the transit.
[d] Raw magnitude values without correction for the quadratic trend in time, or for trends correlated with the shape of the PSF. These are only reported for the follow-up observations.

(This table is available in its entirety in machine-readable form.)

telescopes. Finally, five partial transit events of HATS-35b were obtained between 2015 June 12 and 2015 July 24 using the LCOGT network at CTIO, SAAO, and SSO. The data analysis procedure of these photometric observations has been described comprehensively in previous papers of HATSouth planet discoveries (see, e.g., Brahm et al. 2015; Hartman et al. 2015; Mancini et al. 2015).

We also monitored HATS-34 in the infrared K_S-band during the time of predicted secondary eclipse using the AAT+IRIS2. Observations and data reduction were carried out in the manner described in Zhou et al. (2015). Details of this observation are set out in Table 1, and the observations are used to help rule out blend scenarios in Section 3.2.

2.4. Lucky Imaging Observations

High-spatial-resolution (or "lucky") imaging observations of HATS-31 and HATS-34 candidates were obtained using the Astralux Sur camera on the New Technology Telescope (NTT) at the La Silla Observatory (Hippler et al. 2009). Data were reduced and contrast curves generated as described in Espinoza et al. (2016). We show the resulting combination of the best 10% of the images acquired for each target for HATS-31 and HATS-34 in Figure 4. The resulting images show an asymmetric extended profile for HATS-31 that is visible in all of the Astralux images. This object was observed during twilight and the observations were obtained out of focus. The profile is more symmetric for HATS-34.

In Figure 5, we show the generated $5-\sigma$ contrast curves for HATS-31 and HATS-34. We simulate the point spread function (PSF) for our targets as a weighted sum of a Moffat profile and an asymmetric Gaussian following the model description in Espinoza et al. (2016). The effective full width at half maximum (FWHM) of this model was measured numerically at different angles by finding the points at which the model has half of the peak flux. The median of these measurements is taken as the resolution limit of our observations. For HATS-31, the effective FWHM is 6.58 ± 0.36 pixels, which corresponds to a resolution limit of 151.4 ± 8.3 milli-arcseconds (mas). In the case of HATS-34, the effective FWHM is 4.17 ± 0.33 pixels, which gives a resolution limit of 96.0 ± 7.5 mas.

3. ANALYSIS

3.1. Properties of the Parent Star

To derive the physical properties of their planetary companions, we first obtained the atmospheric parameters of the host stars. We used high-resolution spectra of HATS-31 through HATS-35 obtained with FEROS, together with the Zonal Atmospherical Stellar Parameter Estimator code (ZASPE; Brahm et al. 2016) to determine the effective temperature ($T_{\rm eff\star}$), surface gravity ($\log g_\star$), metallicity ([Fe/H]), and projected equatorial rotation velocity ($v \sin i$) for each star.

$T_{\rm eff\star}$ and [Fe/H] values obtained using ZASPE were used with the stellar density $\rho_\star$, which was determined from the combined light-curve and RV analysis to determine a first estimate of the stellar physical parameters following the method described in Sozzetti et al. (2007). We used the Yonsei-Yale isochrones (Y2; Yi et al. 2001) to search for the parameters (stellar mass, radius, and age) that best match our estimated $T_{\rm eff\star}$, [Fe/H], and $\rho_\star$ values. Based on this comparison, we determine a revised value of $\log g_\star$ and then perform a second iteration of ZASPE, holding $\log g_\star$ fixed to this value while fitting for $T_{\rm eff\star}$ [Fe/H] and $v \sin i$. These are then combined with $\rho_\star$ and once again compared to the Y2 isochrones to produce our final adopted values for the physical stellar parameters.

Table 4
Stellar Parameters for HATS-31, HATS-32 and HATS-33

Parameter	*HATS-31* Value	*HATS-32* Value	*HATS-33* Value	Source
Astrometric properties and cross-identifications				
2MASS-ID	2MASS 12464866-2425385	2MASS 23041801-2116189	2MASS 19383207-5519483	
GSC-ID	GSC 6688-00298	GSC 6400-00924	GSC 8778-01635	
R.A. (J2000)	$12^h46^m48^s.72$	$23^h04^m18^s.12$	$19^h38^m31^s.92$	2MASS
Decl. (J2000)	$-24°25'38''.5$	$-21°16'19''.0$	$-55°19'48''.4$	2MASS
$\mu_{R.A.}$ (mas yr^{-1})	1.2 ± 1.0	2.9 ± 1.9	7.1 ± 1.1	UCAC4
$\mu_{Decl.}$ (mas yr^{-1})	-0.4 ± 1.1	-20.3 ± 1.9	-40.6 ± 1.3	UCAC4
Spectroscopic properties				
$T_{eff\star}$ (K)	6050 ± 120	5700 ± 110	5659 ± 85	ZASPE[a]
[Fe/H]	0.000 ± 0.070	0.390 ± 0.050	0.290 ± 0.050	ZASPE
$v \sin i$ (km s^{-1})	7.01 ± 0.50	3.56 ± 0.69	3.87 ± 0.42	ZASPE
v_{mac} (km s^{-1})	3.90	4.44	5.01	Assumed
v_{mic} (km s^{-1})	1.27	1.04	1.01	Assumed
γ_{RV} (m s^{-1})	-8704.5 ± 8.9	12423 ± 13	11077 ± 12	FEROS or HARPS[b]
Photometric properties				
B (mag)	13.687 ± 0.030	15.106 ± 0.030	12.633 ± 0.070	APASS[c]
V (mag)	13.105 ± 0.030	14.384 ± 0.010	11.911 ± 0.070	APASS[c]
g (mag)	13.356 ± 0.030	14.694 ± 0.010	12.174 ± 0.040	APASS[c]
r (mag)	12.950 ± 0.030	14.130 ± 0.010	11.704 ± 0.040	APASS[c]
i (mag)	12.775 ± 0.080	14.035 ± 0.010	11.52 ± 0.11	APASS[c]
J (mag)	11.912 ± 0.021	13.090 ± 0.022	10.659 ± 0.024	2MASS
H (mag)	11.618 ± 0.025	12.768 ± 0.027	10.337 ± 0.026	2MASS
K_s (mag)	11.572 ± 0.023	12.699 ± 0.033	10.287 ± 0.027	2MASS
Derived properties				
$M_\star$ ($M_\odot$)	1.275 ± 0.096	1.099 ± 0.044	1.062 ± 0.032	YY+$\rho_\star$+ZASPE[d]
$R_\star$ ($R_\odot$)	1.87 ± 0.18	$1.097^{+0.098}_{-0.063}$	$1.022^{+0.050}_{-0.037}$	YY+$\rho_\star$+ZASPE
$\log g_\star$ (cgs)	4.000 ± 0.065	4.396 ± 0.057	4.445 ± 0.036	YY+$\rho_\star$+ZASPE
$\rho_\star$ (g cm^{-3})	$0.275^{+0.082}_{-0.061}$	1.19 ± 0.23	1.42 ± 0.17	Light curves
$\rho_\star$ (g cm^{-3})[e]	$0.275^{+0.082}_{-0.059}$	1.17 ± 0.22	1.40 ± 0.16	YY+Light curves+ZASPE
$L_\star$ ($L_\odot$)	4.16 ± 0.95	$1.14^{+0.24}_{-0.18}$	0.96 ± 0.12	YY+$\rho_\star$+ZASPE
M_V (mag)	3.25 ± 0.24	4.69 ± 0.21	4.89 ± 0.14	YY+$\rho_\star$+ZASPE
M_K (mag,ESO)	1.88 ± 0.21	3.10 ± 0.17	3.270 ± 0.099	YY+$\rho_\star$+ZASPE
Age (Gyr)	4.3 ± 1.1	3.5 ± 1.8	3.0 ± 1.7	YY+$\rho_\star$+ZASPE
A_V (mag)	0.154 ± 0.092	$0.064^{+0.085}_{-0.064}$	0.000 ± 0.058	YY+$\rho_\star$+ZASPE
Distance (pc)	872 ± 84	839^{+77}_{-55}	255 ± 12	YY+$\rho_\star$+ZASPE

Notes. For all three systems, the fixed-circular-orbit model has higher Bayesian evidence than the eccentric-orbit model. We therefore assume a fixed circular orbit in generating the parameters listed for these systems.

[a] ZASPE = Zonal Atmospherical Stellar Parameter Estimator routine for the analysis of high-resolution spectra (Brahm et al. 2016), applied to the HARPS spectra of HATS-31, and the FEROS spectra of the other systems. These parameters rely primarily on ZASPE, but also have a small dependence on the iterative analysis incorporating the isochrone search and global modeling of the data.

[b] From HARPS for HATS-31 and HATS-33 and from FEROS for HATS-32. The error on γ_{RV} is determined from the orbital fit to the velocity measurements, and does not include the systematic uncertainty in transforming the velocities to the IAU standard system. The velocities have not been corrected for gravitational redshifts.

[c] From APASS DR6 (Henden et al. 2009), as listed in the UCAC 4 catalog (Zacharias et al. 2012).

[d] YY+$\rho_\star$+ZASPE = based on the YY isochrones (Yi et al. 2001), $\rho_\star$ as a luminosity indicator, and the ZASPE results.

[e] In the case of $\rho_\star$, we list two values. The first value is determined from the global fit to the light curves and RV data, without imposing a constraint that the parameters match the stellar evolution models. The second value results from restricting the posterior distribution to combinations of $\rho_\star$+$T_{eff\star}$+[Fe/H] that match a YY stellar model.

The adopted parameters for HATS-31, HATS-32, and HATS-33 are given in Table 4, and for HATS-34 and HATS-35 in Table 5. We show the locations of each of the stars on the $T_{eff\star}$–$\rho_\star$ diagram (similar to a Hertzsprung–Russell diagram) in Figure 6. This analysis shows that HATS-31 has a mass of $1.275 \pm 0.096\,M_\odot$, a radius of $1.87 \pm 0.18\,R_\odot$, and an age of 4.3 ± 1.1 Gyr. HATS-32 has a mass of $1.099 \pm 0.044\,M_\odot$, a radius of $1.097^{+0.098}_{-0.063}\,R_\odot$, and an age of 3.5 ± 1.8 Gyr. HATS-33 has a mass of $0.955 \pm 0.031\,M_\odot$, a radius of $0.980 \pm 0.047\,R_\odot$, and an age of 7.7 ± 2.7 Gyr. HATS-34 has a mass of $0.955 \pm 0.031\,M_\odot$, a radius of $0.980 \pm 0.047\,R_\odot$, and an age of 7.7 ± 2.7 Gyr. Finally, HATS-35 has a mass of $1.317 \pm 0.040\,M_\odot$, a radius of $1.433^{+0.056}_{-0.038}\,R_\odot$, and an age of 2.13 ± 0.51 Gyr. Distances for each star are calculated by comparing the broadband photometry of Table 4 to the predicted magnitudes in each filter from the isochrones. To determine the extinction, we assumed a $R_V = 3.1$ extinction law (Cardelli et al. 1989). The distances for these systems range between 255 ± 12 pc to 872 ± 84 pc for HATS-33 and HATS-31, respectively.

Table 5
Stellar Parameters for HATS-34 and HATS-35

Parameter	*HATS-34* Value	*HATS-35* Value	Source
Astrometric properties and cross-identifications			
2MASS-ID	2MASS 00030587-6228096	2MASS 19464518-6333561	
GSC-ID	GSC 8840-01777	GSC 9089-00775	
R.A. (J2000)	$00^h03^m05^s.88$	$19^h46^m45^s.12$	2MASS
Decl. (J2000)	$-62°28'09''.6$	$-63°33'56''.2$	2MASS
$\mu_{\rm R.A.}$ (mas yr^{-1})	2.1±1.4	16.7±1.3	UCAC4
$\mu_{\rm Decl.}$ (mas yr^{-1})	4.7±1.5	−12.1±1.3	UCAC4
Spectroscopic properties			
$T_{\rm eff\star}$ (K)	5380 ± 73	6300 ± 100	ZASPE[a]
[Fe/H]	0.250±0.070	0.210±0.060	ZASPE
$v \sin i$ (km s^{-1})	4.07±0.58	8.66±0.34	ZASPE
$v_{\rm mac}$ (km s^{-1})	3.56	3.83	Assumed
$v_{\rm mic}$ (km s^{-1})	0.88	1.51	Assumed
$\gamma_{\rm RV}$ (m s^{-1})	17735.1±9.3	−14175±13	FEROS or HARPS[b]
Photometric properties			
B (mag)	14.595±0.010	13.26±0.10	APASS[c]
V (mag)	13.849±0.010	12.56±0.10	APASS[c]
g (mag)	14.182±0.010	…	APASS[c]
r (mag)	13.650±0.010	…	APASS[c]
i (mag)	13.459±0.050	…	APASS[c]
J (mag)	12.513±0.024	11.439±0.025	2MASS
H (mag)	12.139±0.022	11.192±0.023	2MASS
K_s (mag)	12.095±0.019	11.118±0.025	2MASS
Derived properties			
$M_\star$ ($M_\odot$)	0.955±0.031	1.317±0.040	YY+$\rho_\star$+ZASPE[d]
$R_\star$ ($R_\odot$)	0.980±0.047	$1.433^{+0.056}_{-0.038}$	YY+$\rho_\star$+ZASPE
$\log g_\star$ (cgs)	4.435±0.043	4.244±0.023	YY+$\rho_\star$+ZASPE
$\rho_\star$ (g cm^{-3})	1.44±0.25	$0.627^{+0.046}_{-0.060}$	Light curves
$\rho_\star$ (g cm^{-3})[e]	1.44±0.22	$0.628^{+0.045}_{-0.061}$	YY+Light Curves+ZASPE
$L_\star$ ($L_\odot$)	0.724±0.089	2.92±0.31	YY+$\rho_\star$+ZASPE
M_V (mag)	5.26±0.15	3.58±0.12	YY+$\rho_\star$+ZASPE
M_K (mag,ESO)	3.41±0.11	2.399±0.073	YY+$\rho_\star$+ZASPE
Age (Gyr)	7.7±2.7	2.13±0.51	YY+$\rho_\star$+ZASPE
A_V (mag)	0.0000±0.0063	0.25±0.14	YY+$\rho_\star$+ZASPE
Distance (pc)	532 ± 32	557^{+22}_{-17}	YY+$\rho_\star$+ZASPE

Notes. For HATS-34 and HATS-35, the fixed-circular-orbit model has higher Bayesian evidence than the eccentric-orbit model. We therefore assume a fixed circular orbit in generating the parameters listed for both systems.

[a] ZASPE = Zonal Atmospherical Stellar Parameter Estimator routine for the analysis of high-resolution spectra (Brahm et al. 2016), applied to the FEROS spectra of each star. These parameters rely primarily on ZASPE, but also have a small dependence on the iterative analysis incorporating the isochrone search and global modeling of the data.

[b] From FEROS for both objects. The error on $\gamma_{\rm RV}$ is determined from the orbital fit to the velocity measurements and does not include the systematic uncertainty in transforming the velocities to the IAU standard system. The velocities have not been corrected for gravitational redshifts.

[c] From APASS DR6 (Henden et al. 2009) as listed in the UCAC 4 catalog (Zacharias et al. 2012).

[d] YY+$\rho_\star$+ZASPE = based on the YY isochrones (Yi et al. 2001), $\rho_\star$ as a luminosity indicator, and the ZASPE results.

[e] In the case of $\rho_\star$, we list two values. The first value is determined from the global fit to the light curves and RV data, without imposing a constraint that the parameters match the stellar evolution models. The second value results from restricting the posterior distribution to combinations of $\rho_\star$+$T_{\rm eff\star}$+ [Fe/H] that match a YY stellar model.

3.2. Excluding Blend Scenarios

In order to exclude blend scenarios, we carried out an analysis following Hartman et al. (2012). We attempt to model the available photometric data (including light curves and catalog broadband photometric measurements) for each object as a blend between an eclipsing binary star system and a third star along the line of sight. The physical properties of the stars are constrained using the Padova isochrones (Girardi et al. 2000), while we also require that the brightest of the three stars in the blend have atmospheric parameters consistent with those measured with ZASPE. We also simulate composite cross-correlation functions (CCFs) and use them to predict velocities and BSs for each blend scenario considered.

Based on this analysis, we rule out blended stellar eclipsing binary scenarios for all five systems. However, in general, we cannot rule out the possibility that one or more of these objects may be an unresolved binary star system with one component hosting a transiting planet. The results for each object are as follows.

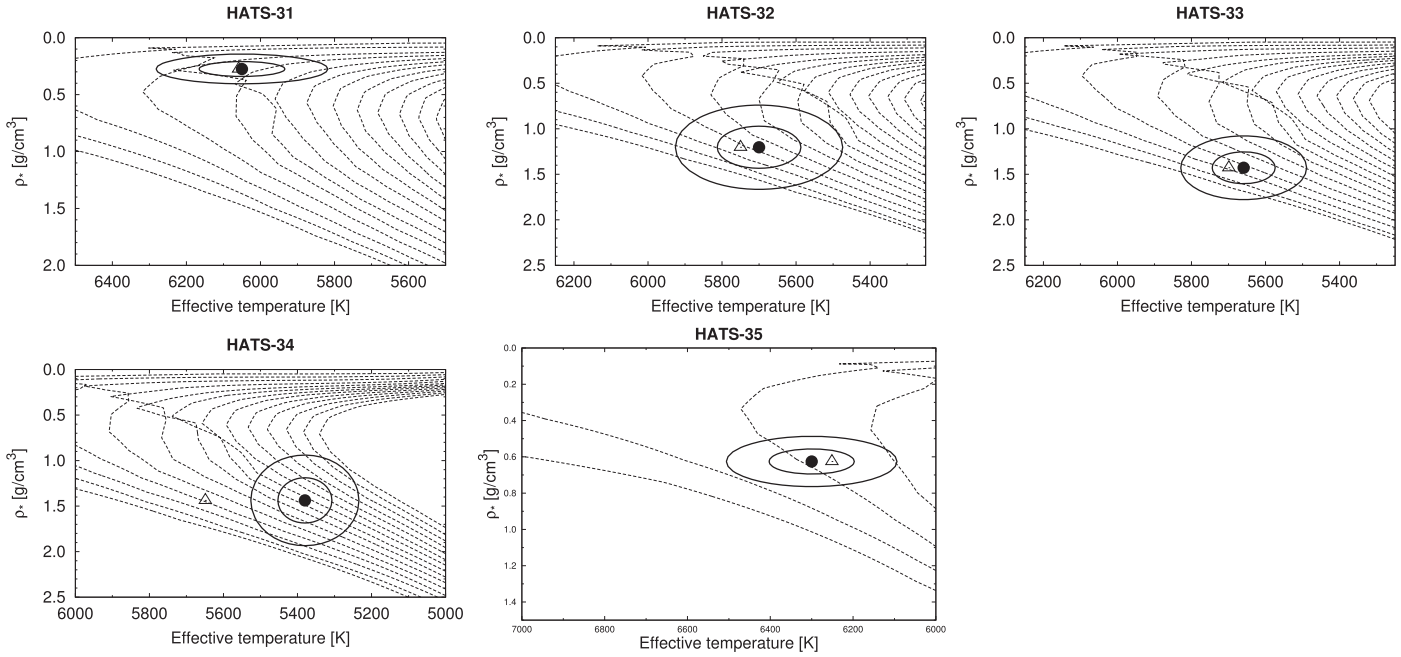

Figure 6. Model isochrones from Yi et al. (2001) for the measured metallicities of each of the five new transiting planet host stars. We show models for ages of 0.2 Gyr (leftmost dashed line), 1.0 Gyr (second dashed line from left), and then models increasing in 1.0 Gyr increments (ages increasing from left to right). The adopted values of $T_{\rm eff\star}$ and $\rho_\star$ are shown by the black circles together with their 1σ and 2σ confidence ellipsoids. The initial values of $T_{\rm eff\star}$ and $\rho_\star$ from the first ZASPE and light-curve analysis are represented with a triangle. In the case of HATS-31, there was little change to the parameter values between the two iterations and the triangle lies partially under the black circle.

1. *HATS-31*: all blend models tested can be rejected with at least 3σ confidence based solely on the photometry. Those blend models that cannot be rejected based on the photometry with at least 5σ confidence predict large amplitude radial valocity and/or BS variations (i.e., greater than $1\,{\rm km\,s^{-1}}$, which is well above what is observed).
2. *HATS-32*: all blend models tested yield higher χ^2, based solely on the photometry, than the model of a single star with a transiting planet. Those blend models that cannot be rejected with 5σ confidence predict either velocity scatter above $200\,{\rm m\,s^{-1}}$ (and a variation that does not look like the observed Keplerian variation), or a BS variation above $300\,{\rm m\,s^{-1}}$.
3. *HATS-33*: all blend models tested can be rejected with at least 3σ confidence based solely on the photometry. Those models that are not rejected with at least 5σ confidence would have been easily identified as composite systems based on the CCFs computed from their spectra.
4. *HATS-34*: all blend models tested can be rejected with at lest 3σ confidence based solely on the photometry. In particular, the best-fit blend model predicts a 5 mmag secondary eclipse in the K_S-band which was not seen in the AAT/IRIS2 observations. Our blend analysis allows for a quadratic trend in the follow-up light curves when fitting the data, and the best-fit model includes a trend that cancels to some degree the predicted secondary eclipse. If we do not allow for such a trend in fitting the data, then the blend models are actually rejected with greater than 5σ confidence. Some of the blend models that are rejected at 4–5σ confidence (when the trend is included) do predict velocity and BS variations that have comparable amplitudes to the observed variations. In detail, however, the simulated blend velocities do not fit the data nearly as well as a single star with a planet. The BS variation is, however, captured somewhat better by the blend model. Nonetheless, given the constraints set by the photometry and radial velocities, we consider the blended stellar eclipsing binary model to be ruled out, and conclude that the observed BS variation must be due to some other cause (e.g., sky contamination or the presence of an unresolved star diluting the transiting planet system).
5. *HATS-35*: all blend models tested can be rejected with greater than 8σ confidence based on the photometry alone. This is primarily driven by the large amplitude out-of-transit variation predicted for blend models capable of fitting the primary transit. The HATSouth light curve strongly excludes any such out-of-transit variation.

3.3. Global Modeling of the Data

We modeled the HATSouth photometry, the follow-up photometry, and the high-precision RV measurements following Pál et al. (2008), Bakos et al. (2010), and Hartman et al. (2012). We fit Mandel & Agol (2002) transit models to the light curves, allowing for a dilution of the HATSouth transit depth as a result of blending from neighboring stars and over-correction by the trend-filtering method. For the follow-up light curves, we include a quadratic trend in time, and linear trends with up to three parameters describing the shape of the PSF in our model for each event to correct for systematic errors in the photometry. We fit Keplerian orbits to the radial velocity data allowing the zero-point for each instrument to vary independently in the fit, and allowing for RV noise, which we also vary as a free parameter for each instrument. We used a Differential

Table 6
Orbital and Planetary Parameters for HATS-31b, HATS-32b, and HATS-33b

Parameter	*HATS-31b* Value	*HATS-32b* Value	*HATS-33b* Value
Light-curve parameters			
P (days)	3.377960±0.000012	2.8126548±0.0000055	2.5495551±0.0000061
T_c (BJD)[a]	2456960.1476±0.0011	2456454.6252±0.0011	2456497.23181±0.00050
T_{14} (days)[a]	0.1914±0.0043	0.1189±0.0036	0.1115±0.0018
$T_{12} = T_{34}$ (days)[a]	0.0202±0.0042	0.0145±0.0025	0.0135±0.0016
$a/R_\star$	5.49±0.43	$7.88^{+0.46}_{-0.61}$	7.83±0.32
$\zeta/R_\star$ [b]	11.67±0.16	19.18±0.52	20.45±0.23
$R_p/R_\star$	0.0908±0.0049	0.1171±0.0039	0.1237±0.0080
b^2	$0.23^{+0.11}_{-0.16}$	$0.16^{+0.12}_{-0.10}$	$0.107^{+0.081}_{-0.065}$
$b \equiv a\cos i/R_\star$	$0.48^{+0.11}_{-0.21}$	$0.40^{+0.13}_{-0.16}$	$0.33^{+0.11}_{-0.12}$
i (deg)	$85.0^{+2.5}_{-1.6}$	87.1±1.2	87.62±0.92
HATSouth blend factors[c]			
Blend factor	0.648±0.071	0.822±0.068	0.769±0.099
Limb-darkening coefficients[d]			
c_1, R	…	0.3723	…
c_2, R	…	0.3122	…
c_1, r	0.3000	0.4005	0.4016
c_2, r	0.3587	0.3061	0.3030
c_1, i	0.2195	0.2989	0.3013
c_2, i	0.3558	0.3243	0.3193
RV parameters			
K (m s^{-1})	102 ± 13	124 ± 14	170.1±6.8
e[e]	<0.233	<0.471	<0.080
RV jitter FEROS (m s^{-1})[f]	…	27 ± 14	<86.5
RV jitter HARPS (m s^{-1})	<0.1	…	<19.2
RV jitter Coralie (m s^{-1})	…	…	46 ± 31
RV jitter CYCLOPS2 (m s^{-1})	…	…	19.4±7.2
Planetary parameters			
M_p (M_J)	0.88±0.12	0.92±0.10	1.192±0.053
R_p (R_J)	1.64±0.22	$1.249^{+0.144}_{-0.096}$	$1.230^{+0.112}_{-0.081}$
$C(M_p, R_p)$[g]	0.10	0.12	0.03
ρ_p (g cm^{-3})	$0.243^{+0.124}_{-0.088}$	0.58±0.16	0.79±0.19
$\log g_p$ (cgs)	2.90±0.12	3.158±0.092	3.289±0.072
a (au)	0.0478±0.0012	0.04024±0.00053	0.03727±0.00037
$T_{\rm eq}$ (K)	1823±81	1437±58	1429±38
Θ[h]	0.0396±0.0079	0.0531±0.0076	0.0675±0.0061
$\log_{10}\langle F\rangle$ (cgs)[i] …	9.397±0.076	8.984±0.070	8.973±0.046

Notes. For all three systems, the fixed-circular-orbit model has a higher Bayesian evidence than the eccentric-orbit model. We therefore assume a fixed circular orbit in generating the parameters listed for these systems.

[a] Times are in Barycentric Julian Date calculated directly from UTC without correction for leap seconds. T_c: reference epoch of mid-transit that minimizes the correlation with the orbital period. T_{14}: total transit duration, time between first to last contact; $T_{12} = T_{34}$: ingress/egress time, time between first and second, or third and fourth contact.

[b] Reciprocal of the half duration of the transit used as a jump parameter in our Markov chain Monte Carlo (MCMC) analysis in place of $a/R_\star$. It is related to $a/R_\star$ by the expression $\zeta/R_\star = a/R_\star(2\pi(1 + e\sin\omega))/(P\sqrt{1-b^2}\sqrt{1-e^2})$ (Bakos et al. 2010).

[c] Scaling factor applied to the model transit that is fit to the HATSouth light curves. This factor accounts for dilution of the transit due to blending from neighboring stars and over-filtering of the light curve. These factors are varied in the fit, and we allow independent factors for observations obtained with different HATSouth camera and field combinations.

[d] Values for a quadratic law, adopted from the tabulations by Claret (2004) according to the spectroscopic (ZASPE) parameters listed in Table 4.

[e] For fixed-circular-orbit models, we list the 95% confidence upper limit on the eccentricity determined when $\sqrt{e}\cos\omega$ and $\sqrt{e}\sin\omega$ are allowed to vary in the fit.

[f] Term added in quadrature to the formal RV uncertainties for each instrument. This is treated as a free parameter in the fitting routine. In cases where the jitter is consistent with zero, we list the 95% confidence upper limit.

[g] Correlation coefficient between the planetary mass M_p and radius R_p estimated from the posterior parameter distribution.

[h] The Safronov number is given by $\Theta = \frac{1}{2}(V_{\rm esc}/V_{\rm orb})^2 = (a/R_p)(M_p/M_\star)$ (see Hansen & Barman 2007).

[i] Incoming flux per unit surface area, averaged over the orbit.

Evolution Markov Chain Monte Carlo procedure to explore the fitness landscape and to determine the posterior distribution of the parameters. Note that we tried fitting both fixed-circular-orbits and free-eccentricity models to the data. We estimate the Bayesian evidence for the fixed-circular and free-eccentricity models for each system, and find that for HATS-31b through HATS-35b the fixed-circular-orbit models have higher evidence than the free-eccentricity models. For these systems, we

Table 7
Orbital and Planetary Parameters for HATS-34b and HATS-35b

Parameter	*HATS-34b* Value	*HATS-35b* Value
Light-curve parameters		
P (days)	2.1061607 ± 0.0000047	1.8209993 ± 0.0000016
T_c (BJD)[a]	$2456634.85732 \pm 0.00075$	$2456981.80199 \pm 0.00041$
T_{14} (days)[a]	0.0648 ± 0.0029	0.1299 ± 0.0010
$T_{12} = T_{34}$ (days)[a]	0.081 ± 0.011	0.01314 ± 0.00083
$a/R_\star$	6.96 ± 0.34	$4.79^{+0.11}_{-0.16}$
$\zeta/R_\star$ [b]	61 ± 11	17.13 ± 0.11
$R_p/R_\star$	0.150 ± 0.014	0.1051 ± 0.0012
b^2	$0.879^{+0.041}_{-0.063}$	$0.068^{+0.066}_{-0.054}$
$b \equiv a \cos i/R_\star$	$0.937^{+0.022}_{-0.034}$	$0.26^{+0.11}_{-0.14}$
i (deg)	$82.28^{+0.43}_{-0.59}$	86.9 ± 1.3
HATSouth blend factors[c]		
Blend factor	0.822 ± 0.086	1 ± 0
Limb-darkening coefficients[d]		
c_1, R	0.4277	…
c_2, R	0.2728	…
c_1, r	0.4588	0.2746
c_2, r	0.2646	0.3780
c_1, i	…	0.1962
c_2, i	…	0.3739
RV parameters		
K (m s^{-1})	152 ± 11	170 ± 10
e[e]	<0.108	<0.306
ω (deg)	…	0 ± 0
$\sqrt{e}\cos\omega$ (deg)	…	0 ± 0
$\sqrt{e}\sin\omega$ (deg)	…	0 ± 0
$e\cos\omega$ (deg)	…	0 ± 0
$e\sin\omega$ (deg)	…	0 ± 0
RV jitter FEROS (m s^{-1})[f]	<31.3	<50.5
RV jitter HARPS (m s^{-1})	…	<96.3
RV jitter Coralie (m s^{-1})	…	2 ± 52
Planetary parameters		
M_p (M_J)	0.941 ± 0.072	1.222 ± 0.078
R_p (R_J)	1.43 ± 0.19	$1.464^{+0.069}_{-0.044}$
$C(M_p, R_p)$ [g]	-0.00	0.18
ρ_p (g cm^{-3})	$0.40^{+0.19}_{-0.13}$	$0.484^{+0.042}_{-0.070}$
$\log g_p$ (cgs)	3.05 ± 0.12	$3.151^{+0.025}_{-0.053}$
a (au)	0.03166 ± 0.00034	0.03199 ± 0.00033
$T_{\rm eq}$ (K)	1445 ± 42	2037 ± 43
Θ [h]	0.0430 ± 0.0068	$0.0405^{+0.0020}_{-0.0036}$
$\log_{10}\langle F\rangle$ (cgs)[i]	8.994 ± 0.050	9.590 ± 0.037

Notes. For HATS-34 and HATS-35, the fixed-circular-orbit model has higher Bayesian evidence than the eccentric-orbit model.

[a] Times are in Barycentric Julian Date calculated directly from UTC without correction for leap seconds. T_c: reference epoch of mid-transit that minimizes the correlation with the orbital period. T_{14}: total transit duration, time between first to last contact; $T_{12} = T_{34}$: ingress/egress time, time between first and second, or third and fourth contact.

[b] Reciprocal of the half duration of the transit used as a jump parameter in our MCMC analysis in place of $a/R_\star$. It is related to $a/R_\star$ by the expression $\zeta/R_\star = a/R_\star(2\pi(1 + e\sin\omega))/(P\sqrt{1-b^2}\sqrt{1-e^2})$ (Bakos et al. 2010).

[c] Scaling factor applied to the model transit that is fit to the HATSouth light curves. This factor accounts for dilution of the transit due to blending from neighboring stars and over-filtering of the light curve. These factors are varied in the fit, and we allow independent factors for observations obtained with different HATSouth camera and field combinations. For HATS-35, we run TFA in signal-reconstruction mode and have also confirmed that there are no diluting neighbors on the HATSouth images. We therefore fix the blend factor to unity for this system.

[d] Values for a quadratic law, adopted from the tabulations by Claret (2004) according to the spectroscopic (ZASPE) parameters listed in Table 5.

[e] For fixed-circular-orbit models, we list the 95% confidence upper limit on the eccentricity determined when $\sqrt{e}\cos\omega$ and $\sqrt{e}\sin\omega$ are allowed to vary in the fit.

[f] Term added in quadrature to the formal radial velocity uncertainties for each instrument. This is treated as a free parameter in the fitting routine. In cases where this noise term is consistent with zero, we list the 95% confidence upper limit.

[g] Correlation coefficient between the planetary mass M_p and radius R_p estimated from the posterior parameter distribution.

[h] The Safronov number is given by $\Theta = \frac{1}{2}(V_{\rm esc}/V_{\rm orb})^2 = (a/R_p)(M_p/M_\star)$ (see Hansen & Barman 2007).

[i] Incoming flux per unit surface area, averaged over the orbit.

Table 8
Relative Radial Velocities and Bisector Spans for HATS-31–HATS-35

Star	BJD (2,450,000+)	RV[a] (m s^{-1})	σ_{RV}[b] (m s^{-1})	BS (m s^{-1})	σ_{BS} (m s^{-1})	Phase	Instrument
			HATS-31				
HATS-31	7067.77200	68.51	29.00	−8.0	58.0	0.861	HARPS
HATS-31	7068.80731	−111.49	22.00	138.0	44.0	0.167	HARPS
HATS-31	7069.83756	5.51	35.00	98.0	66.0	0.472	HARPS
HATS-31	7070.78858	89.51	22.00	64.0	44.0	0.754	HARPS
HATS-31	7071.81170	−38.49	15.00	34.0	32.0	0.057	HARPS
HATS-31	7072.81373	−87.49	18.00	46.0	40.0	0.353	HARPS
			HATS-32				
HATS-32	6857.88391	−65.26	11.00	−2.0	15.0	0.373	FEROS
HATS-32	6858.83608	142.74	11.00	43.0	16.0	0.712	FEROS
HATS-32	7183.82218	−157.26	23.00	−13.0	30.0	0.256	FEROS
HATS-32	7184.92441	96.74	16.00	47.0	22.0	0.648	FEROS
HATS-32	7186.82299	−67.26	20.00	61.0	26.0	0.323	FEROS
HATS-32	7187.92768	119.74	13.00	−43.0	18.0	0.716	FEROS
HATS-32	7189.81850	−121.26	13.00	−22.0	18.0	0.388	FEROS
HATS-32	7190.90671	102.74	13.00	−18.0	18.0	0.775	FEROS
			HATS-33				
HATS-33	7109.90663	−115.04	11.00	16.0	18.0	0.307	Coralie
HATS-33	7118.90238	150.99	7.00	1.0	28.0	0.835	HARPS
HATS-33	7119.85968	−166.01	9.00	−22.0	38.0	0.211	HARPS
HATS-33	7120.89565	120.99	6.00	−2.0	24.0	0.617	HARPS
HATS-33	7150.22296	−94.90	12.00	⋯	⋯	0.120	CYCLOPS2
HATS-33	7150.23892	−138.80	12.40	⋯	⋯	0.126	CYCLOPS2
HATS-33	7150.25487	−101.70	12.60	⋯	⋯	0.133	CYCLOPS2
HATS-33	7151.26648	56.90	11.80	⋯	⋯	0.529	CYCLOPS2
HATS-33	7151.28183	62.40	14.80	⋯	⋯	0.535	CYCLOPS2
HATS-33	7151.29714	54.70	12.20	⋯	⋯	0.541	CYCLOPS2
HATS-33	7152.18422	87.60	10.40	⋯	⋯	0.889	CYCLOPS2
HATS-33	7152.19954	81.50	8.60	⋯	⋯	0.895	CYCLOPS2
HATS-33	7152.21486	75.50	7.40	⋯	⋯	0.901	CYCLOPS2
HATS-33	7156.17139	−38.60	19.80	⋯	⋯	0.453	CYCLOPS2
HATS-33	7156.18735	−57.70	17.20	⋯	⋯	0.459	CYCLOPS2
HATS-33	7166.75718	119.88	10.00	13.0	14.0	0.605	FEROS
HATS-33	7179.83946	219.96	13.00	5.0	22.0	0.736	Coralie
HATS-33	7180.77062	−154.04	14.00	53.0	24.0	0.102	Coralie
HATS-33	7181.85831	17.96	14.00	41.0	22.0	0.528	Coralie
HATS-33	7182.81335	123.96	13.00	34.0	22.0	0.903	Coralie
HATS-33	7187.78052	160.88	10.00	4.0	12.0	0.851	FEROS
HATS-33	7187.79155	132.88	10.00	12.0	11.0	0.855	FEROS
HATS-33	7212.69884	59.88	12.00	−63.0	17.0	0.625	FEROS
			HATS-34				
HATS-34	7181.90516	156.41	12.00	16.0	17.0	0.737	FEROS
HATS-34	7188.87902	−25.59	17.00	16.0	23.0	0.048	FEROS
HATS-34	7211.86173	16.41	14.00	−20.0	19.0	0.960	FEROS
HATS-34	7222.87045	−161.59	15.00	−147.0	20.0	0.187	FEROS
HATS-34	7223.79478	85.41	19.00	−53.0	25.0	0.626	FEROS
HATS-34	7224.81561	−62.59	18.00	−10.0	24.0	0.111	FEROS
HATS-34	7229.67888	−83.59	12.00	−92.0	16.0	0.420	FEROS
			HATS-35				
HATS-35	6971.53689	−83.38	41.00	−61.0	29.0	0.363	Coralie
HATS-35	7119.91638	116.74	30.00	99.0	27.0	0.846	HARPS
HATS-35	7120.91245	−119.26	17.00	−38.0	18.0	0.393	HARPS
HATS-35	7179.85943[d]	400.62	44.00	⋯	⋯	0.763	Coralie
HATS-35	7180.79013	−129.38	53.00	⋯	38.0	0.274	Coralie
HATS-35	7181.87795	87.62	46.00	⋯	35.0	0.872	Coralie
HATS-35	7182.85998	−153.38	47.00	⋯	35.0	0.411	Coralie
HATS-35	7190.83382	224.82	22.00	67.0	14.0	0.790	FEROS
HATS-35	7191.72420	−155.18	20.00	36.0	14.0	0.279	FEROS

Table 8
(Continued)

Star	BJD (2,450,000+)	RV[a] (m s^{-1})	σ_{RV}[b] (m s^{-1})	BS (m s^{-1})	σ_{BS} (m s^{-1})	Phase	Instrument
HATS-35	7192.65831	209.82	21.00	58.0	14.0	0.792	FEROS
HATS-35	7196.92836	−124.18	24.00	60.0	16.0	0.137	FEROS
HATS-35	7218.84882	−112.18	22.00	91.0	15.0	0.174	FEROS
HATS-35	7223.62885	170.82	25.00	91.0	17.0	0.799	FEROS
HATS-35	7224.52818	−131.18	22.00	50.0	15.0	0.293	FEROS
HATS-35	7226.86401	14.82	23.00	−41.0	15.0	0.576	FEROS
HATS-35	7229.85682	−170.18	23.00	1.0	15.0	0.219	FEROS
HATS-35	7230.84273	178.82	18.00	35.0	12.0	0.761	FEROS

Notes.
[a] The zero-point of these velocities is arbitrary. An overall offset γ_{rel} fitted independently to the velocities from each instrument has been subtracted.
[b] Internal errors excluding the component of astrophysical jitter considered in Section 3.3.

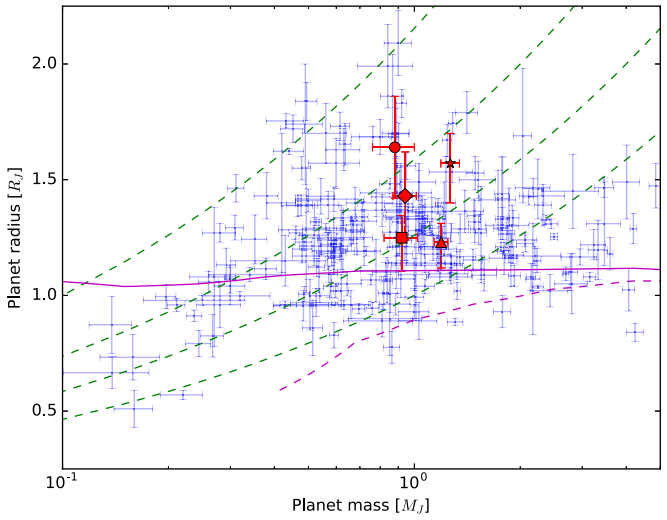

Figure 7. Mass-radius diagram of all known transiting hot Jupiters, i.e., planets with masses of $0.1M_J < M < 5M_J$ and periods $P < 10$ days, with precisely measured masses and radii from the NASA Exoplanet Archive. HATS-31b is shown with a red circle, HATS-32b with a red square, HATS-33b with a red triangle, HATS-34b with a red diamond, and HATS-35b with a red star. The green dashed lines show isodensity curves with densities of 0.1, 0.25, 0.5, and 1 ρ_J. Theoretical mass–radius relations of 4.5 Gyr old planets for irradiated planets at 0.045 au from the host star from Fortney et al. (2007) are shown by magenta lines for core-free giant planets (solid line) and for planets with 100 $M_\oplus$ cores (dashed line).

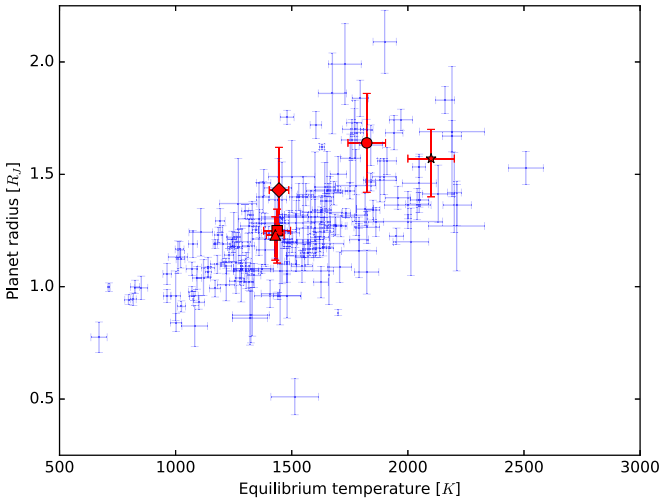

Figure 8. Planet equilibrium temperature versus radius for the same sample of transiting hot Jupiters plotted in the mass–radius diagram. HATS-31b through HATS-35b are represented with the same symbols as in Figure 7.

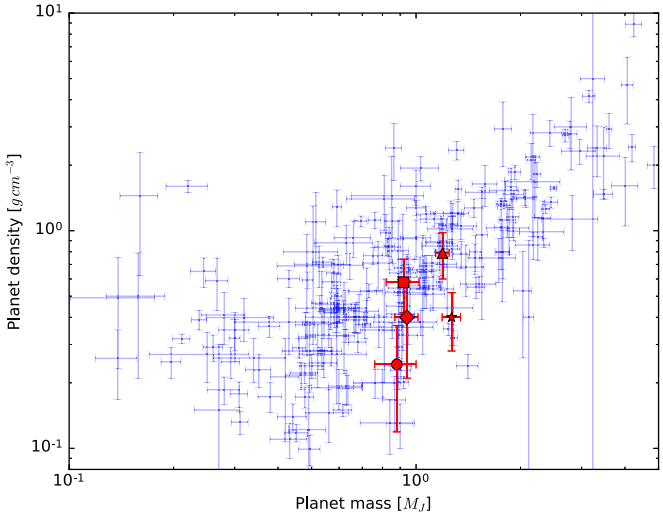

Figure 9. Mass–density diagram of all known transiting hot Jupiters, planets with masses of $0.1M_J < M < 5M_J$ and periods $P < 10$ days with well-characterized masses and radii, taken from the NASA Exoplanet Archive. Red data points as per Figure 7.

therefore adopt the parameters that come from the fixed-circular-orbit models. The resulting parameters for HATS-31b, HATS-32b, and HATS-33b are listed in Table 6, while for HATS-34b and HATS-35b they are listed in Table 7.

HATS-31b, HATS-32b, and HATS-34b have a mass that is smaller than Jupiter, between $0.88 \pm 0.12\,M_J$ and $0.941 \pm 0.072\,M_J$, whereas the other two objects are slightly more massive than Jupiter. All planets have radii larger than Jupiter within the range $1.230^{+0.112}_{-0.081}$ to $1.64 \pm 0.22\,R_J$. These planets are moderately irradiated hot Jupiters with HATS-31b and HATS-35b having relatively high equilibrium temperatures of 1823 ± 81 K and 2037 ± 43 K, respectively.

4. DISCUSSION

We have presented five new transiting hot Jupiters, HATS-31b through to HATS-35b, discovered by the HATSouth

survey. Our analysis of the combined photometric and spectroscopic data rules out the possibility that these transit detections are blended stellar eclipsing binary systems, and we conclude that these objects are transiting planets. In Figure 7, we show the mass–radius and versus radius diagrams of all known transiting hot Jupiters with well determined masses and radii discovered to date retrieved from the NASA Exoplanet Archive[16] on 2016 May 30, with HATS-31b through HATS-35b superimposed in red. The theoretical mass–radius relations are shown for core-free giant planets and for planets with 100 $M_{\oplus}$ cores for irradiated planets at 0.045 au from the host star, which is roughly appropriate for the insolation levels received by HATS-31b to HATS-35b (Fortney et al. 2007).

From the mass–radius diagram shown in Figure 7, the planets presented in this paper can be classified as typical hot Jupiters in terms of their masses and radii. HATS-31b, HATS-32b, and HATS-34b are slightly less massive than Jupiter with $0.88 \pm 0.12\,M_{\rm J}$, $0.92 \pm 0.10\,M_{\rm J}$, and $0.941 \pm 0.072\,M_{\rm J}$, respectively. However, the radius values of the five objects, all higher than that of Jupiter, vary between $1.230^{+0.112}_{-0.081}\,R_{\rm J}$ for HATS-33b to $1.64 \pm 0.22\,R_{\rm J}$ for HATS-31b. The planet equilibrium temperature versus radius diagram is shown in Figure 8. The equilibrium temperature of the planets presented in this paper agree with previously observed general trends. HATS-31b and HATS-35b have higher equilibrium temperature, in the range of 1823 ± 81 K to 2037 ± 43 K, compared with the other three objects presented here.

It can be seen from the mass–radius and equilibrium temperature-radius diagrams that HATS-31b and HATS-35b reside in a different region than the other three planets. HATS-31b and HATS-35b have radii of $1.64 \pm 0.22\,R_{\rm J}$ and $1.464^{+0.069}_{-0.044}\,R_{\rm J}$, respectively, and are therefore moderately inflated planets, while HATS-32b, HATS-33b, and HATS-34b have radii from 1.2 $R_{\rm J}$ to 1.4 $R_{\rm J}$, which is close to the mean radius of known hot Jupiters. This indicates that the inflated radii are linked to the increased irradiation from their parent star. All of the discovered planets have a period below the mean value of transiting hot Jupiters, with the shortest period of the sample being 1.8209993 ± 0.0000016 days for HATS-35b.

In Figure 9, we show the planet density against mass for HATS-31b–HATS-35b in the context of all known exoplanets with well-characterized densities. HATS-31b is the lowest density planet of the objects presented in this paper, with a mean density of $0.243^{+0.124}_{-0.088}$ g cm^{-3}, while the other objects have typical densities between $0.484^{+0.042}_{-0.070}$ g cm^{-3} and 0.79 ± 0.19 g cm^{-3}, for objects of their mass and period.

Development of the HATSouth project was funded by NSF MRI grant NSF/AST-0723074. Operations have been supported by NASA grants NNX09AB29G and NNX12AH91-H and follow-up observations receive partial support from grant NSF/AST-1108686. A.J. acknowledges support from FONDECYT project 1130857, BASAL CATA PFB-06, and project IC120009 "Millennium Institute of Astrophysics (MAS)" of the Millenium Science Initiative, Chilean Ministry of Economy. R.B. and N.E. are supported by CONICYT-PCHA/Doctorado Nacional. R.B. and N.E. acknowledge additional support from project IC120009 "Millenium Institute of Astrophysics (MAS)" of the Millennium Science Initiative, Chilean Ministry of Economy. V.S. acknowledges support form BASAL CATA PFB-06. M.R. acknowledges support from FONDECYT postdoctoral fellowship 3120097. This work is based on observations made with ESO Telescopes at the La Silla Observatory. This paper also uses observations obtained with facilities of the Las Cumbres Observatory Global Telescope. Work at the Australian National University is supported by ARC Laureate Fellowship Grant FL0992131. We acknowledge the use of the AAVSO Photometric All-Sky Survey (APASS), funded by the Robert Martin Ayers Sciences Fund, and the SIMBAD database, operated at CDS, Strasbourg, France. Operations at the MPG 2.2 m Telescope are jointly performed by the Max Planck Gesellschaft and the European Southern Observatory. We thank the MPG 2.2 m Telescope support crew for their technical assistance during observations. We are grateful to P. Sackett for her help in the early phase of the HATSouth project. G.B. wishes to thank the warm hospitality of Adele and Joachim Cranz at the farm Isabis, supporting the operations and service missions of HATSouth. Observing times were obtained through proposals CN2013A-171, CN2013B-55, CN2014A-104, CN2014B-57, CN2015A-51, and ESO 096.C-0544. This research has made use of the NASA Exoplanet Archive, which is operated by the California Institute of Technology under contract with the National Aeronautics and Space Administration under the Exoplanet Exploration Program.

[16] http://exoplanetarchive.ipac.caltech.edu/

REFERENCES

Addison, B. C., Tinney, C. G., Wright, D. J., et al. 2013, ApJL, 774, L9
Bakos, G., Noyes, R. W., Kovács, G., et al. 2004, PASP, 116, 266
Bakos, G. Á., Csubry, Z., Penev, K., et al. 2013, PASP, 125, 154
Bakos, G. Á., Torres, G., Pál, A., et al. 2010, ApJ, 710, 1724
Barge, P., Baglin, A., Auvergne, M., et al. 2008, A&A, 482, L17
Bayliss, D., Zhou, G., Penev, K., et al. 2013, AJ, 146, 113
Borucki, W. J., Koch, D., Basri, G., et al. 2010, Sci, 327, 977
Brahm, R., Jordan, A., Hartman, J., & Bakos, G. 2016, arXiv:1607.05792
Brahm, R., Jordán, A., Hartman, J. D., et al. 2015, AJ, 150, 33
Brown, T. M., Baliber, N., Bianco, F. B., et al. 2013, PASP, 125, 1031
Cardelli, J. A., Clayton, G. C., & Mathis, J. S. 1989, ApJ, 345, 245
Claret, A. 2004, A&A, 428, 1001
Espinoza, N., Bayliss, D., Hartman, J. D., et al. 2016, arXiv:1606.00023
Fortney, J. J., Marley, M. S., & Barnes, J. W. 2007, ApJ, 659, 1661
Girardi, L., Bressan, A., Bertelli, G., & Chiosi, C. 2000, A&AS, 141, 371
Hansen, B. M. S., & Barman, T. 2007, ApJ, 671, 861
Hartman, J. D., Bakos, G. Á., Béky, B., et al. 2012, AJ, 144, 139
Hartman, J. D., Bayliss, D., Brahm, R., et al. 2015, AJ, 149, 166
Henden, A. A., Welch, D. L., Terrell, D., & Levine, S. E. 2009, in AAS Meeting 214 Abstracts, #407
Hippler, S., Bergfors, C., Wolfgang, Brandner., et al. 2009, Msngr, 137, 14
Horton, A., Tinney, C. G., Case, S., et al. 2012, Proc. SPIE, 8446, 84463A
Jordán, A., Brahm, R., Bakos, G. Á., et al. 2014, AJ, 148, 29
Kaufer, A., & Pasquini, L. 1998, Proc. SPIE, 3355, 844
Kovács, G., Bakos, G., & Noyes, R. W. 2005, MNRAS, 356, 557
Kovács, G., Zucker, S., & Mazeh, T. 2002, A&A, 391, 369
Mancini, L., Hartman, J. D., Penev, K., et al. 2015, A&A, 580, A63
Mandel, K., & Agol, E. 2002, ApJL, 580, L171
Mayor, M., Pepe, F., Queloz, D., et al. 2003, Msngr, 114, 20
Pál, A., Bakos, G. Á., Torres, G., et al. 2008, ApJ, 680, 1450
Penev, K., Bakos, G. Á., Bayliss, D., et al. 2013, AJ, 145, 5
Penev, K. M., Hartman, J. D., Bakos, G. A., et al. 2016, arXiv:1606.00848
Pollacco, D. L., Skillen, I., Collier Cameron, A., et al. 2006, PASP, 118, 1407
Queloz, D., Mayor, M., Udry, S., et al. 2001, Msngr, 105, 1
Siverd, R. J., Beatty, T. G., Pepper, J., et al. 2012, ApJ, 761, 123
Sozzetti, A., Torres, G., Charbonneau, D., et al. 2007, ApJ, 664, 1190
Yi, S., Demarque, P., Kim, Y.-C., et al. 2001, ApJS, 136, 417
Zacharias, N., Finch, C. T., Girard, T. M., et al. 2012, yCat, 1322, 0
Zhou, G., Bayliss, D. D. R., Kedziora-Chudczer, L., et al. 2015, MNRAS, 454, 3002